

# Common origin of the pseudogap in electron-doped and hole-doped cuprates governed by Mott physics

M. Horio<sup>1</sup>, S. Sakai<sup>2</sup>, K. Koshiishi<sup>1</sup>, Y. Nonaka<sup>1</sup>, H. Suzuki<sup>1</sup>, J. Xu<sup>1</sup>, M. Hashimoto<sup>3</sup>, D. Lu<sup>3</sup>,  
Z.-X. Shen<sup>3</sup>, T. Ohgi<sup>4</sup>, T. Konno<sup>4</sup>, T. Adachi<sup>5</sup>, Y. Koike<sup>4</sup>, M. Imada<sup>6</sup> and A. Fujimori<sup>1</sup>

<sup>1</sup>*Department of Physics, University of Tokyo, Bunkyo-ku, Tokyo 113-0033, Japan*

<sup>2</sup>*Center for Emergent Matter Science, RIKEN, Wako, Saitama 351-0198, Japan*

<sup>3</sup>*Stanford Synchrotron Radiation Lightsource, SLAC National Accelerator Laboratory, Menlo Park, California 94305, USA*

<sup>4</sup>*Department of Applied Physics, Tohoku University, Sendai 980-8579, Japan*

<sup>5</sup>*Department of Engineering and Applied Sciences, Sophia University, Tokyo 102-8554, Japan and*

<sup>6</sup>*Department of Applied Physics, University of Tokyo, Bunkyo-ku, Tokyo 113-0033, Japan*

(Dated: October 28, 2021)

The pseudogap phenomena have been a long-standing mystery of the cuprate high-temperature superconductors. Unlike the pseudogap in hole-doped cuprates, however, the pseudogap in the electron-doped counterpart has been attributed to band folding due to short-range antiferromagnetic (AFM) order. We performed angle-resolved photoemission spectroscopy measurements on electron-doped cuprates showing spin-glass and disordered AFM behaviors at low temperatures, and found that the gap magnitude *decreases* in the antinodal region contrary to the hole-doped case. Moreover, the gap opening position was not always on the AFM Brillouin zone boundary in contradiction with the requirement of the AFM band-folding picture. These features are consistent with cluster dynamical-mean-field-theory calculations which predict an *s*-symmetry pseudogap that shrinks in the antinodal region. The present results support the scenario that the proximity to the Mott insulator, without relying on the AFM correlation, gives rise to a momentum-dependent pseudogap of *s*-symmetry with indirect gap commonly in the electron-doped and hole-doped cuprates, implying a universal origin of the pseudogap with a similarity to the Mott gap formation.

One of the most unusual and intriguing features of the cuprate superconductors is the pseudogap phenomena. So far, a variety of proposals have been made as the origin of the pseudogap. Among them, preformed Cooper pairs [1] and competing orders such as charge order [2] and nematic order [3, 4] have been extensively discussed. Another scenario is the proximity to the Mott insulator, which does not rely on any competing orders and hence is compatible with the universality of the pseudogap. Cluster dynamical-mean-field-theory (CDMFT) calculations based on the Hubbard model for hole-doped cuprates are consistent with this scenario, where a pseudogap of *s*-symmetry opens between split quasi-particle (QP) bands in the entire momentum space [5, 6]. The split QP bands mostly reside on the unoccupied side of the Fermi level ( $E_F$ ) except for the antinodal region, where the lower band moves to below  $E_F$  so that the pseudogap becomes detectable by angle-resolved photoemission spectroscopy (ARPES). Such a highly electron-hole asymmetric pseudogap has been detected by an ARPES experiment at relatively high temperatures covering a few tens meV above  $E_F$  [7] and an electronic Raman scattering experiment [6]. However, ARPES cannot access the major part of the pseudogap in the hole-doped cuprates, which extends up to several hundreds meV above  $E_F$ . In the present work, we have made detailed ARPES measurements on electron-doped cuprates, where the major part of the pseudogap appears below  $E_F$  and is accessible by ARPES.

The pseudogap of the electron-doped cuprates has been

observed through the measurements of optical conductivity [8, 9], scanning tunneling spectroscopy [10], and ARPES [11–18]. Its origin has been considered to be disordered antiferromagnetism since the spectral intensity is strongly suppressed around the “hot spot”, where the Fermi surface and the AFM Brillouin zone (BZ) boundary cross each other. If a mean-field-type AFM band folding gives rise to the pseudogap, the band folding should occur across the AFM BZ boundary. Moreover, the magnitude of the gap  $\Delta_{AF}$  should be constant along the AFM BZ boundary. However, an ARPES study by Matsui *et al.* [12] has shown that  $\Delta_{AF}$  decreases with approaching the antinodal region on the AFM BZ boundary. Ikeda *et al.* [16] have also concluded from the band structure observed by ARPES that  $\Delta_{AF}$  becomes zero around  $(\pi, 0)$  and  $(0, \pi)$ . Park *et al.* [13] interpreted their ARPES results so that  $\Delta_{AF}$  is constant throughout the momentum space but is apparently reduced around  $(\pi, 0)$  because antiferromagnetism is inhomogeneous and short ranged.

Most of theoretical studies, either with weak-coupling [19] or strong-coupling treatment [20], have not explicitly shown the momentum dependence of the AFM gap, whereas a variational Monte-Carlo study based on the two-dimensional  $t$ - $t'$ - $t''$ - $J$  model by Chou and Lee [21] has shown that  $\Delta_{AF}$  decreases as one goes from the hot spot to  $(\pi, 0)$ . The deviation of the band structure from the simple band-folding picture should contain important information about electron correlation to understand the pseudogap phenomena not only in the hole-doped cuprates, but also in the electron-doped cuprates. However, com-

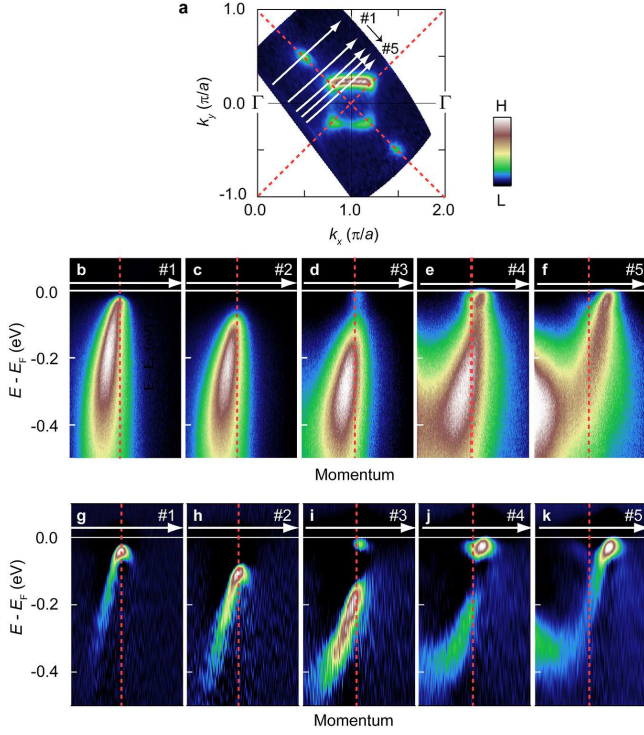


**Figure 1. ARPES spectra of a protect-annealed PLCCO ( $x = 0.02$ ) single crystal.** **a**, Fermi surface mapping. Spectral intensity integrated within  $\pm 20$  meV of  $E_F$  is plotted. **b-f**, Band images taken along the cuts indicated in (a). The AFM BZ boundary is shown by dashed red lines in each panel. **g-k**, Corresponding second derivatives with respect to energy.

parison of hole- and electron-doped cuprates to extract universal features of the pseudogap formation has not been pursued with theoretical examinations.

In this Article, we report on an ARPES study of the electron-doped cuprate  $\text{Pr}_{1.3-x}\text{La}_{0.7}\text{Ce}_x\text{CuO}_4$  (PLCCO,  $x = 0.02$ ) showing spin-glass and disordered AFM behaviors at low temperatures. The sample was protect-annealed under strongly reducing condition to efficiently remove excess oxygen [22]. We have investigated the band structure along various directions in momentum space, and found that the pseudogap is indeed strongly momentum dependent and becomes invisible in the antinodal region. Furthermore, the momentum position of the gap was found to deviate from the AFM BZ boundary around the antinode, which is incompatible with AFM pictures of the pseudogap. The results are consistent with CDMFT calculations, and support the scenario that the proximity to the Mott insulating state universally gives rise to the  $s$ -symmetry pseudogap both for the hole- and electron-doped cuprates as if they are miniaturized Mott gaps.

Figure 1 shows the Fermi surface, band images, and their second derivatives with respect to energy of a protect-annealed PLCCO ( $x = 0.02$ ) sample. The band

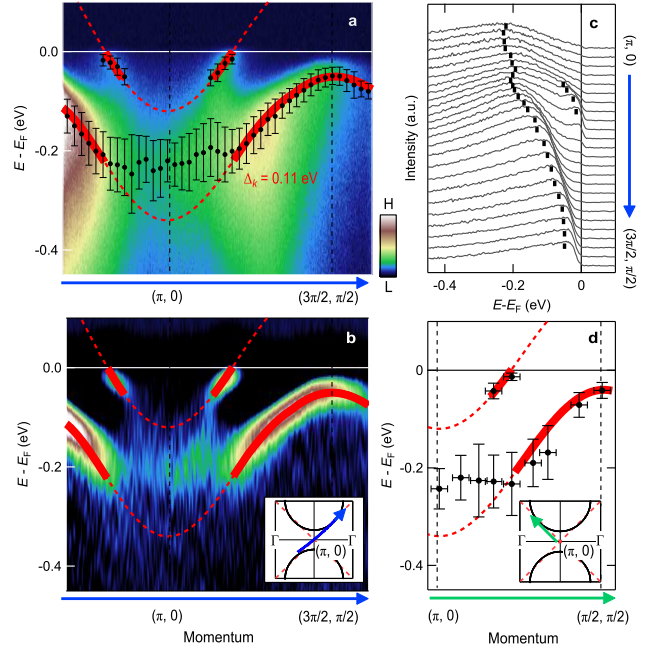


**Figure 2. Band splitting measured along the folded BZ boundary.** **a,b**, Band image and its second derivative with respect to energy along the cut indicated in the inset of **b**. Peak positions of the EDCs are plotted as black dots in **a**. The error bar is defined by the lower-energy-edge width at half maximum ( $\times 33\%$ ). Band dispersions fitted to the mean-field-type model for a  $\mathbf{Q} = (\pi, \pi)$  order with  $\Delta_k = 0.11$  eV (red curves) are also plotted, in which the region relevant to the fitting is represented by solid curves (outside the antinodal region). **c**, EDCs plotted along the folded BZ boundary from  $(\pi, 0)$  to  $(3\pi/2, \pi/2)$  with black bars representing peak positions. **d**, Peak positions of EDCs from  $(\pi/2, \pi/2)$  to  $(\pi, 0)$  extracted from the measurements along several cuts parallel to the  $(0, 0)$ - $(\pi, \pi)$  direction. Band dispersions calculated using the mean-field-type model with the same parameters as above are superimposed, indicating that the band dispersions shown in **b** and **d** are identical.

is gapped at  $E_F$  at the node (cut #1), and the gap below  $E_F$  increases in going from the node to the hot spot (cut #2). On approaching the antinode, the upper split band is lowered below  $E_F$  and produces a finite spectral intensity at and below  $E_F$ . These features are characteristics of the electron-doped cuprates as have been reported in previous studies [12–18].

Now we look into more detail of the band structure. At the node and the hot spot (cuts #1 and #2), as the band disperses from higher binding energy toward  $E_F$ , it disperses back to higher binding energy beyond the AFM BZ boundary, producing a local band maximum at the AFM BZ boundary (Figs. 1g and h) as if the band is folded by the  $\mathbf{Q} = (\pi, \pi)$  AFM order. Once the upper band is lowered below  $E_F$  (cuts #3, #4, and #5), however, the lower band is no longer folded and disperses straightly across the AFM BZ boundary.

The experimentally obtained band image along the AFM BZ boundary, its second derivative with respect to energy, and energy distribution curves (EDCs) are, respectively, shown in Figs. 2a–c. Starting from  $(3\pi/2, \pi/2)$ , the peak position of the EDC shifts smoothly toward higher binding energy, but stops dispersing when the spectral intensity of the upper band emerges below  $E_F$ . Once the upper band reaches the binding energy of  $\sim 50$  meV, the magnitude of the gap decreases, the QP peak widths increase, and the two peaks become unresolved around  $(\pi, 0)$ . Resulting spectra around  $(\pi, 0)$  are considerably broad and incoherent. Qualitatively consistent ARPES spectra were also obtained for a protect-annealed PLCCO sample with  $x = 0.05$ , which exhibits superconductivity as well as lower magnetic ordering temperature (See Supplementary Note 1 and Supplementary Fig. 1).

Closely examining the low-energy spectra around  $(\pi, 0)$  plotted in Figs. 3b–d, one finds that the gap opens away from the AFM BZ boundary. This is in contrast to the nodal region where the band energy position is maximized near the AFM BZ boundary and thus the gap apparently opens around it (cuts #1 and #2). The peculiar momentum dependence of the gap opening positions is summarized in Fig. 3e.

In order to describe these unusual band dispersions, we first try to employ mean-field-type folded bands on the square lattice with a  $\mathbf{Q} = (\pi, \pi)$  order [12, 13, 16], where transfer integrals between the nearest-neighbor ( $t$ ), second-nearest-neighbor ( $t'$ ), and third-nearest-neighbor ( $t''$ ) Cu sites are considered. In the mean-field picture, the potential difference between the two sub-lattices,  $2\Delta_k$ , is constant along the folded BZ boundary, and cannot explain the observed strong momentum dependence.

Assuming phenomenologically different types of bands between around  $(3\pi/2, \pi/2)$  (finite  $\Delta_k$ ) and around  $(\pi, 0)$  (without  $\Delta_k$ ), we have fitted the band dispersions along the folded BZ to the mean-field-type model. Hopping parameters and the chemical potential were set to be identical between the two regions. The best fit obtained with the parameters of  $t = 0.25$  eV,  $t'/t = -0.15$ , and  $t''/t' = -0.5$  is plotted in Figs. 2a, b, and 3b–d by solid curves in the region relevant to the fitting.  $\Delta_k = 0.11$  eV yielded the best fit around  $(3\pi/2, \pi/2)$  while  $\Delta_k \sim 0$  eV better reproduces the band dispersion around  $(\pi, 0)$ . The rapid collapse of the order parameter  $\Delta_k$  cannot be justified within the mean-field-type ordering picture. These mean-field analyses thus seriously fail in understanding the experimental data as we shall discuss in more detail later, although they are still useful for quantifying the band structure.

The electron concentration  $n_{FS}$  was estimated from the Fermi surface area to be 0.104, which is considerably larger than the nominal Ce concentration of  $x = 0.02$ . This Fermi surface area estimated assuming a folded electron-like Fermi surface is consistent with that esti-

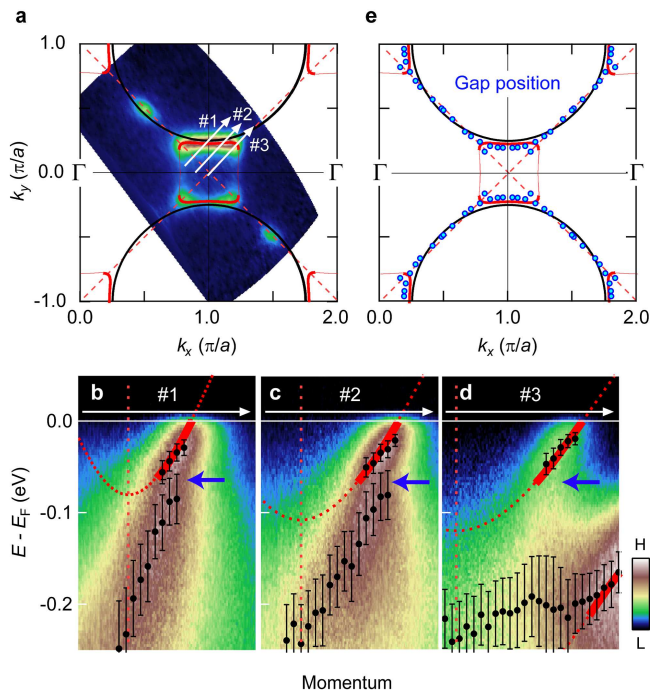


**Figure 3. Low-energy band structure around  $(\pi, 0)$ .** **a**, Fermi surface mapping with the Fermi surface contour calculated using the mean-field-type model with  $\Delta_k = 0$  eV (black curves) and with  $\Delta_k = 0.11$  eV (red curves). **b–d**, Band images along cuts #1–#3 indicated in **a**, respectively. Peak positions of the EDCs are plotted with black dots. The definition of the error bar is the same as in Fig. 2. The bands calculated using the mean-field-type model are also plotted. The lower mean-field bands obtained in the fitting shown in Figs. 2a and b disperse far outside of panels b–d. A gap opens away from the AFM BZ boundary as indicated by blue arrows. **e**, Momentum position of the gap opening. Near  $(\pi/2, \pi/2)$  where only the lower band is visible, it has been defined as the lower band top. In the antinodal part, it has been determined from the momentum-distribution-curve peak in between the upper and lower bands.

mated from unfolded hole-like Fermi surface obtained by tracking the remnant intensity at  $E_F$  [23]. Such excess electrons compared to the nominal Ce content are due to oxygen vacancies resulting from the strong reduction of protect annealing as reported by recent ARPES studies [18]. The observed magnitude of the pseudogap around  $(3\pi/2, \pi/2)$  ( $\Delta_k = 0.11$  eV) is comparable to that of  $\text{Sm}_{2-x}\text{Ce}_x\text{CuO}_4$  ( $x = 0.14, n_{FS} = 0.13$ ) reported in a previous ARPES study [13] in spite of smaller  $n_{FS}$  for the present PLCCO. This can be attributed either to the effect of protect annealing or to the difference in the rare-earth element as the pseudogap magnitude of  $R_{2-x}\text{Ce}_x\text{CuO}_4$  is known to decrease with increasing ionic radius of the rare earth  $R$  [16].

In order to see possible effects of photoionization matrix elements, we have also examined the band dispersion along the folded BZ boundary in a different direction,

from  $(\pi, 0)$  to  $(\pi/2, \pi/2)$ . As plotted in Fig. 2d, the observed band dispersions are identical to the dispersions from  $(\pi, 0)$  to  $(3\pi/2, \pi/2)$  (Figs. 2a and b). The present results thus highlight the momentum dependence of the band splitting and the spectral feature in the electron-doped cuprates: the large pseudogap and sharp spectra around  $(\pi/2, \pi/2)$  and the reduced pseudogap and broad spectra near  $(\pi, 0)$ . This momentum dependence of the pseudogap magnitude is opposite to the ARPES observation for the hole-doped cuprates where the pseudogap is large around  $(\pi, 0)$  and is apparently closed around  $(\pi/2, \pi/2)$  in the occupied spectra below  $E_F$ .

Now, we discuss serious difficulties contained in the above mean-field analysis based on the AFM order. Although the above analysis using the tight-binding model helps us to characterize and quantify the momentum-dependent pseudogap phenomenologically, it requires the abrupt collapse of the order parameter ( $\Delta_k$ ) around  $(\pi, 0)$ . This collapse itself indicates the breakdown of the mean-field picture and hence that the present pseudogap cannot originate from the AFM order. The key aspects of the experimental results are the absence of band folding and of the spectral-weight suppression across the folded BZ boundary in the antinodal lower band (Figs. 1f and g). Even more important is the gap opening away from the folded BZ boundary in the antinodal region (Figs. 3b–d). While the gap positions nearly trace the AFM BZ boundary around  $(\pi/2, \pi/2)$ , they deviate from the AFM BZ boundary on approaching  $(\pi, 0)$  as shown in Fig 3e. These spectral features are incompatible with AFM scenarios and rather suggest a non-AFM origin of the pseudogap.

One scenario to explain the overall band structure without assuming the long-range AFM order is the  $s$ -symmetry pseudogap recently proposed by Sakai *et al.* [5, 6]. From CDMFT calculations based on the Hubbard model, they have shown for the hole-doped cuprates that the pseudogap of  $s$ -symmetry opens in the entire momentum space due to the proximity to a Mott insulator. Both split bands, namely, the QP band originating from the lower Hubbard band and the in-gap states induced just above it, reside above  $E_F$  around  $(\pi/2, \pi/2)$  while around  $(\pi, 0)$  the lower band (QP band) disperses to below  $E_F$  [left panel of Fig. 4a]. More precisely, the size of the gap is smaller around  $(\pi/2, \pi/2)$  than around  $(\pi, 0)$ . Here, the in-gap states are the low-energy electron addition (removal) states induced by hole (electron) doping. Since unoccupied states cannot be detected by ARPES, a pseudogap of hole-doped cuprates is observed predominantly around the antinode. In order to see its connection to the electron-doped case, we shift the chemical potential from the lower Hubbard band to the upper Hubbard band as shown in Fig. 4a. The in-gap states are now induced just below the upper Hubbard band. In the right panel of Fig. 4a, which describes the electron-doped case, both

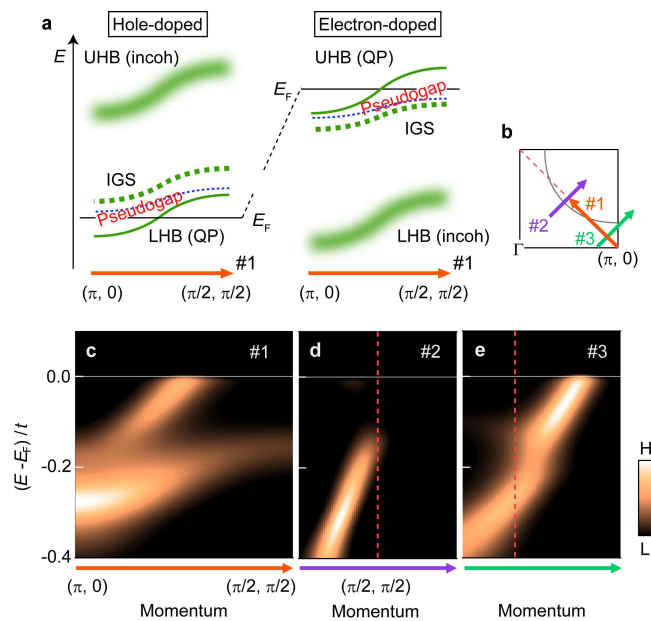


**Figure 4. Cluster dynamical-mean-field-theory (CDMFT) calculation for the electron-doped cuprates.** **a**, Schematic band dispersions along the AFM BZ boundary [cut #1 in panel **b**] for the hole-doped and electron-doped cuprates with the  $s$ -symmetry pseudogap. QP, incoh, UHB, LHB, and IGS represent the quasi-particle band, the incoherent band, the upper Hubbard band, the lower Hubbard band, and in-gap states, respectively. Note that the LHB (incoh) is equivalent to the Zhang-Rice singlet band. The in-gap states are induced just above the lower Hubbard band in the hole-doped cuprates, while they are induced just below the upper Hubbard band in the electron-doped ones. Blue dashed curves represent the maximal point of the imaginary part of the self-energy (“hidden Fermion”) at each momentum. CDMFT calculations yield smaller pseudogap around  $(\pi/2, \pi/2)$  [ $(\pi, 0)$ ] for hole [electron]-doped cuprates. **b**, Momentum cuts for **c**, **d**, and **e**. **c-e**, Spectral function calculated by CDMFT along cuts #1-#3 indicated in panel **b**. See text for details of the calculation.

split bands are occupied around the antinode in contrast to the hole-doped case while only the lower one is occupied around the node, reproducing the present experimental results. The fully gapped structure at the node cannot be accounted for by the  $d$ -wave gap with particle-hole symmetry expected from the pairing precursor.

Following the above consideration, we have carried out  $2 \times 2$  CDMFT calculations of the Hubbard model for the paramagnetic state using parameters  $n = 0.11$ ,  $t' = -0.3t$ , and  $U = 8t$ , where  $n (> 0)$  is the doped electron concentration and  $U$  is the on-site Coulomb repulsion.  $n$  has been set close to the value deduced from the observed Fermi surface area  $n_{FS} = 0.104$ . The  $t'/t$  value has been derived from density-functional-theory calculation [16]. The  $U/t$  value of 8 is in accordance with the theoretical estimate for hole-doped cuprates ( $U/t = 9.5-10.5$ ) using the multi-scale *ab initio* scheme for correlated elec-

trons (MACE) [24], with considering a similar or slightly smaller  $U/t$  value for electron-doped cuprates [25]. Note that the choice of a smaller  $U/t = 6.5$  also yields qualitatively similar result with a somewhat smaller pseudogap (See Supplementary Fig. 2). The obtained spectral function has been multiplied by the Fermi-Dirac function and resolution-broadened for comparison with the ARPES spectra.

The spectral function calculated along the AFM BZ boundary plotted in Fig. 4c indicates that the pseudogap shrinks on approaching  $(\pi, 0)$ , which explains the experimental results (Fig. 2). The electron-concentration dependence of the calculated spectra is also qualitatively consistent with the experimental results (See Supplementary Figs. 3–5). More remarkable is that the calculated antinodal spectrum in Fig. 4e reproduces the essential characteristics (cut #5 in Fig. 1, cuts #1 and #2 in Fig. 3) that the lower band is not folded at the AFM BZ boundary but disperses across it, and the gap opens apart from the AFM BZ boundary. The overall momentum positions of the gap opening (Fig. 3e) is also reproduced satisfactorily (see Supplementary Fig. 6). The antinodal spectra shown in Figs. 3b–d indicate that the upper band loses intensity and the pseudogap opens once it reaches the binding energy of  $\sim 50$  meV, which cannot be explained by the mean-field-type AFM picture. Within the present CDMFT framework, this can be understood as a consequence of hybridization between the QPs and a “hidden Fermion” [blue dashed curve in Fig. 4a] only weakly dispersing around 50 meV below  $E_F$  [26]. “Hidden Fermion” is a phenomenologically introduced fermionic excitation whose dispersion traces the maximal point of the imaginary part of the self-energy [26]. The nodal spectra (Fig. 4d) also lose intensity across the AFM BZ boundary in a similar manner to the corresponding ARPES spectra (cut #1 in Fig. 1).

The overall consistency between the paramagnetic CDMFT result and the ARPES spectra is found in i) the  $s$ -symmetry gap, ii) the electron-hole asymmetry, iii) the reduction of the gap in the antinodal region, iv) the absence of band folding and spectral-weight suppression across the AFM BZ boundary, and v) the gap opening away from the AFM BZ boundary. Mean-field-type AFM order can satisfy points i) and ii), and the variational Monte-Carlo study of the two-dimensional  $t$ - $t'$ - $t''$ - $J$  model by Chou and Lee [21], which was carried out for the AFM ordered state, reproduced the reduction of the pseudogap magnitude around  $(\pi, 0)$  [point iii)]. However, points iv) and v) are our crucial finding and not reproduced by the calculation assuming the AFM order. Note that in the CDMFT calculations, the AFM order is absent. This implies that the pseudogap of electron-doped cuprates originates not from the AFM ordering but from the Mott physics, as has been proposed for the hole-doped cuprates [5, 6]. The present results thus lead to a unified

view of the particle-hole asymmetric pseudogap formation in the cuprates, regardless of the carrier type, without relying on any sort of competing orders such as charge [2], AFM [27], and nematic order [3, 4]. Although the size is much smaller, the momentum dependence of the gap structure (Fig. 2) with an indirect gap (cut #5 in Fig. 1, cuts #1 and #2 in Fig. 3) shows a remarkable resemblance with the Mott gap as one sees in Fig. 4a (See Supplementary Fig. 3 for the calculated spectral function including the unoccupied side), in contrast to the direct gap expected in the case of the AFM gap.

Whereas the aforementioned variational Monte-Carlo study of the two-dimensional  $t$ - $t'$ - $t''$ - $J$  model by Chou and Lee [21] was carried out for the AFM ordered state, our CDMFT calculation has been conducted for the paramagnetic state but short-range AFM correlations have been taken into account. Despite some differences between these two calculations, qualitative similarity of the momentum dependences except for the existence/absence of band folding suggests a universal mechanism of the reduced splitting in the antinodal region. Since both of the split bands are located above  $E_F$  in the nodal region of the hole-doped case and below  $E_F$  of the electron-doped case in the antinodal region, these momentum regions do not gain the energy by the gap opening. This commonly accounts for the diminished gaps in both cases which leads to the opposite momentum dependences. The CDMFT calculations thus reproduce the key experimental difference of the pseudogap around  $(\pi, 0)$  between the hole- and electron-doped cuprates: large pseudogap in the former and diminishing pseudogap in the latter. It should be noted that this momentum dependence is clearly unrelated to the precursor of  $d$ -wave superconductivity, which must be symmetric with respect to  $E_F$ . The enhanced gap in the nodal region of the electron-doped cuprates is also interpreted as a stronger hybridization strength with the “hidden Fermion”, as a consequence of emergent self-organization to lower the energy [26].

Recently, it has been demonstrated that the superconducting transition temperature  $T_c$  of electron-doped cuprates have a doping dependence similar to that of the hole-doped cuprates when the doping level is evaluated from the Fermi surface area  $n_{FS}$  measured by ARPES [23], and the renewed cuprate phase diagram looks more electron-hole symmetric than previously thought. The present study has further elucidated that the Mott physics is the common origin of the pseudogaps observed in the electron- and hole-doped cuprates. These new findings will allow a unified understanding for both types of cuprates from a new perspective. Deeper understanding of the similar momentum dependences of the Mott gap and the pseudogaps of the hole-doped and electron-doped cuprates will be an intriguing future issue.

In conclusion, we have carried out ARPES measurements on the non-superconducting protect-annealed

electron-doped cuprate PLCCO ( $x = 0.02$ ) which shows spin-glass behavior and disordered antiferromagnetism at low temperatures, and investigated the nature of the “antiferromagnetic” pseudogap. By examining the band structure in the wide momentum range, we have revealed that the magnitude of the pseudogap is strongly momentum dependent and is reduced around  $(\pi, 0)$ . The results are qualitatively explained by a CDMFT calculation based on the Hubbard model, according to which the pseudogap shows a minimum around  $(\pi, 0)$  and the spectra in that momentum region do not show band folding. This agreement suggests that the Mott physics is at the origin of the pseudogap formation in the electron-doped cuprates, and supports the scenario that an  $s$ -symmetry pseudogap arises in the cuprates commonly to the Mott insulating gap from the same underlying physics.

## Methods

### Sample preparation

Single crystals of PLCCO with  $x = 0.02$  were synthesized by the traveling-solvent floating-zone method. First the sample was protect-annealed at 850 °C for 24 hours and then annealed at 400 °C for 48 hours. Annealing generally suppresses the QP scattering rate [28] and sharpens ARPES spectra [15, 17, 18], which enables us to determine the band structure precisely. The annealed  $x = 0.02$  sample showed metallic behavior at high temperatures, but was not superconducting. According to muon-spin-rotation ( $\mu$ SR) measurements, the sample showed disordered antiferromagnetism below 140 K. Furthermore, the magnetic susceptibility showed difference between field cooling and zero-field cooling below  $\sim 15$  K, indicative of a spin-glass behavior [29] (See Supplementary Note 2 and Supplementary Fig. 7). Note that the  $\mu$ SR measurements have been conducted on samples annealed at slightly lower temperatures. Specifically, they were protect-annealed at 825 °C for 24 hours and then annealed at 400 °C for 48 hours. Judging from the shorter  $c$ -axis lattice parameter, the removal of impurity apical oxygen atoms [30] was more thoroughly made for the samples for the ARPES and magnetic susceptibility measurements, and hence the AFM order was more strongly suppressed.

### ARPES measurements

ARPES measurements were carried out at beamline 5-4 of Stanford Synchrotron Radiation Lightsource. Circularly polarized light with  $h\nu = 16.5$  eV was used. The total energy resolution was set at 15 meV. The sample was cleaved *in-situ* under pressure better than  $3 \times 10^{-11}$  Torr and measured at 10 K.

### CDMFT calculation

CDMFT calculation was performed with  $2 \times 2$  interacting cluster coupled to eight bath sites. The cluster impurity

problem was solved with the exact diagonalization method at zero temperature. The spectra were calculated with an energy-broadening factor  $0.05t$  and a cumulant-interpolation technique [31] in momentum space.

## Acknowledgements

Fruitful discussion with T. K. Lee, D. Song, and C. Kim is gratefully acknowledged. ARPES measurements were performed at the Stanford Synchrotron Radiation Lightsource, operated by the Office of Basic Energy Science, US Department of Energy. This work was supported by Grants-in-aid from the Japan Society of the Promotion of Science (JSPS) (grant Nos. 14J09200, 15H02109, 16H06345, 16K05458, 17H02915, and 17K14350). M.H. acknowledges financial support from the Advanced Leading Graduate Course for Photon Science (ALPS) and the JSPS Research Fellowship for Young Scientists. M.I. thanks the RIKEN Advanced Institute for Computational Science through the HPCI System Research project “Creation of new functional devices and high-performance materials to support next-generation industries” (CDMSI) under the project number hp170263.

## Author contributions

M. Horio, K.K., Y.N., H.S., and J.X. performed ARPES measurements with the assistance of M. Hashimoto. ARPES endstation was maintained by M. Hashimoto, D.L., and Z.-X.S. M. Horio analyzed the data. S.S. and M.I. performed CDMFT calculations. T.O., T.K., T.A., and Y.K. synthesized and characterized single crystals. M. Horio and A.F. wrote the manuscript with suggestions by S.S., M.I., T.A., and Y.K. All authors contributed to the scientific planning and discussions. A.F. was responsible for overall project direction and planning.

## Competing financial interests

The authors declare no competing financial interests.

- 
- [1] Emery, V. J. & Kivelson, S. A. Importance of phase fluctuations in superconductors with small superfluid density. *Nature (London)* **374**, 434 (1995).
  - [2] Comin, R. *et al.* Charge Order Driven by Fermi-Arc Instability in  $\text{Bi}_2\text{Sr}_{2-x}\text{La}_x\text{CuO}_{6+\delta}$ . *Science* **343**, 390–392 (2014).
  - [3] Hinkov, V. *et al.* Electronic Liquid Crystal State in the High-Temperature Superconductor  $\text{YBa}_2\text{Cu}_3\text{O}_{6.45}$ . *Science* **319**, 597 (2008).
  - [4] Lawler, M. J. *et al.* Intra-unit-cell electronic nematicity of the high- $T_c$  copper-oxide pseudogap states. *Nature (London)* **466**, 347 (2010).
  - [5] Sakai, S., Motome, Y. & Imada, M. Doped high- $T_c$  cuprate superconductors elucidated in the light of zeros

- and poles of the electronic Green's function. *Phys. Rev. B* **82**, 134505 (2010).
- [6] Sakai, S. *et al.* Raman-Scattering Measurements and Theory of the Energy-Momentum Spectrum for Underdoped  $\text{Bi}_2\text{Sr}_2\text{CaCuO}_{8+\delta}$  Superconductors: Evidence of an  $s$ -Wave Structure for the Pseudogap. *Phys. Rev. Lett.* **111**, 107001 (2013).
- [7] Yang, H.-B. *et al.* Emergence of preformed Cooper pairs from the doped Mott insulating state in  $\text{Bi}_2\text{Sr}_2\text{CaCu}_2\text{O}_{8+\delta}$ . *Nature* **456**, 77 (2008).
- [8] Onose, Y. *et al.* Doping Dependence of Pseudogap and Related Charge Dynamics in  $\text{Nd}_{2-x}\text{Ce}_x\text{CuO}_4$ . *Phys. Rev. Lett.* **87**, 217001 (2001).
- [9] Wang, N. L. *et al.* Doping evolution of the chemical potential, spin-correlation gap, and charge dynamics of  $\text{Nd}_{2-x}\text{Ce}_x\text{CuO}_4$ . *Phys. Rev. B* **73**, 184502 (2006).
- [10] Zimmers, A. *et al.* Local tunneling spectroscopy of the electron-doped cuprate superconductor  $\text{Sm}_{1.85}\text{Ce}_{0.15}\text{CuO}_4$ . *Phys. Rev. B* **76**, 132505 (2007).
- [11] Armitage, N. P. *et al.* Anomalous Electronic Structure and Pseudogap Effects in  $\text{Nd}_{1.85}\text{Ce}_{0.15}\text{CuO}_4$ . *Phys. Rev. Lett.* **87**, 147003 (2001).
- [12] Matsui, H. *et al.* Angle-Resolved Photoemission Spectroscopy of the Antiferromagnetic Superconductor  $\text{Nd}_{1.87}\text{Ce}_{0.13}\text{CuO}_4$ : Anisotropic Spin-Correlation Gap, Pseudogap, and the Induced Quasiparticle Mass Enhancement. *Phys. Rev. Lett.* **94**, 047005 (2005).
- [13] Park, S. R. *et al.* Electronic structure of electron-doped  $\text{Sm}_{1.86}\text{Ce}_{0.14}\text{CuO}_4$ : Strong pseudogap effects, nodeless gap, and signatures of short-range order. *Phys. Rev. B* **75**, 060501 (2007).
- [14] Matsui, H. *et al.* Evolution of the pseudogap across the magnet-superconductor phase boundary of  $\text{Nd}_{2-x}\text{Ce}_x\text{CuO}_4$ . *Phys. Rev. B* **75**, 224514 (2007).
- [15] Richard, P. *et al.* Competition between Antiferromagnetism and Superconductivity in the Electron-Doped Cuprates Triggered by Oxygen Reduction. *Phys. Rev. Lett.* **99**, 157002 (2007).
- [16] Ikeda, M. *et al.* Effects of chemical pressure on the Fermi surface and band dispersion of the electron-doped high- $T_c$  superconductors. *Phys. Rev. B* **80**, 014510 (2009).
- [17] Song, D. *et al.* Oxygen-content-dependent electronic structures of electron-doped cuprates. *Phys. Rev. B* **86**, 144520 (2012).
- [18] Horio, M. *et al.* Suppression of the antiferromagnetic pseudogap in the electron-doped high-temperature superconductor by protect annealing. *Nat. Commun.* **7**, 10567 (2016).
- [19] Kyung, B. *et al.* Pseudogap and Spin Fluctuations in the Normal State of the Electron-Doped Cuprates. *Phys. Rev. Lett.* **93**, 147004 (2004).
- [20] S en echal, D. & Tremblay, A.-M. S. Hot Spots and Pseudogaps for Hole- and Electron-Doped High-Temperature Superconductors. *Phys. Rev. Lett.* **92**, 126401 (2004).
- [21] Chou, C.-P. & Lee, T.-K. Variational approach to strong correlation in the photoemission of electron-doped superconductors. *J. Phys. Chem. Solids* **69**, 2944 – 2948 (2008).
- [22] Adachi, T. *et al.* Evolution of the Electronic State through the Reduction Annealing in Electron-Doped  $\text{Pr}_{1.3-x}\text{La}_{0.7}\text{Ce}_x\text{CuO}_{4+\delta}$  ( $x = 0.10$ ) Single Crystals: Antiferromagnetism, Kondo Effect, and Superconductivity. *J. Phys. Soc. Jpn.* **82**, 063713 (2013).
- [23] Song, D. *et al.* Electron Number-Based Phase Diagram of  $\text{Pr}_{1-x}\text{LaCe}_x\text{CuO}_{4-\delta}$  and Possible Absence of Disparity between Electron- and Hole-Doped Cuprate Phase Diagrams. *Phys. Rev. Lett.* **118**, 137001 (2017).
- [24] Hirayama, M. *et al.* Ab initio effective hamiltonians for cuprate superconductors. *Phys. Rev. B* **98**, 134501 (2018).
- [25] Jang, S. W. *et al.* Direct theoretical evidence for weaker correlations in electron-doped and hg-based hole-doped cuprates. *Sci. Rep.* **6**, 33397 (2016).
- [26] Sakai, S., Civelli, M. & Imada, M. Hidden Fermionic Excitation Boosting High-Temperature Superconductivity in Cuprates. *Phys. Rev. Lett.* **116**, 057003 (2016).
- [27] Motoyama, E. M. *et al.* Spin correlations in the electron-doped high-transition-temperature superconductor  $\text{Nd}_{2-x}\text{Ce}_x\text{CuO}_{4\pm\delta}$ . *Nature (London)* **445**, 186 (2007).
- [28] Xu, X. Q. *et al.* Oxygen dependence of the transport properties of  $\text{Nd}_{1.78}\text{Ce}_{0.22}\text{CuO}_{4\pm\delta}$ . *Phys. Rev. B* **53**, 871–875 (1996).
- [29] Kuroshima, S. *et al.* Phase diagram of the electron-doped superconductor  $\text{Pr}_{1-x}\text{LaCe}_x\text{CuO}_{4-\delta}$ . *Physica C: Superconductivity* **392**, 216 – 220 (2003).
- [30] Radaelli, P. G. *et al.* Evidence of apical oxygen in  $\text{Nd}_2\text{CuO}_y$  determined by single-crystal neutron diffraction. *Phys. Rev. B* **49**, 15322–15326 (1994).
- [31] Stanescu, T. D. & Kotliar, G. Fermi arcs and hidden zeros of the Green function in the pseudogap state. *Phys. Rev. B* **74**, 125110 (2006).

# Supplementary Information

## Common origin of the pseudogap in electron-doped and hole-doped cuprates governed by Mott physics

M. Horio<sup>1</sup>, S. Sakai<sup>2</sup>, K. Koshiishi<sup>1</sup>, Y. Nonaka<sup>1</sup>, H. Suzuki<sup>1</sup>, J. Xu<sup>1</sup>, M. Hashimoto<sup>3</sup>, D. Lu<sup>3</sup>, Z.-X. Shen<sup>3</sup>, T. Ohgi<sup>4</sup>, T. Konno<sup>4</sup>, T. Adachi<sup>5</sup>, Y. Koike<sup>4</sup>, M. Imada<sup>6</sup> and A. Fujimori<sup>1</sup>

<sup>1</sup>*Department of Physics, University of Tokyo, Bunkyo-ku, Tokyo 113-0033, Japan*

<sup>2</sup>*Center for Emergent Matter Science, RIKEN, Wako, Saitama 351-0198, Japan*

<sup>3</sup>*Stanford Synchrotron Radiation Lightsource, SLAC National Accelerator Laboratory, Menlo Park, California 94305, USA*

<sup>4</sup>*Department of Applied Physics, Tohoku University, Sendai 980-8579, Japan*

<sup>5</sup>*Department of Engineering and Applied Sciences, Sophia University, Tokyo 102-8554, Japan*

<sup>6</sup>*Department of Applied Physics, University of Tokyo, Bunkyo-ku, Tokyo 113-0033, Japan*

\*e-mail: horio@physik.uzh.ch



## Supplementary Notes

### Supplementary Note 1: Physical properties and ARPES spectra of $\text{Pr}_{1.3-x}\text{La}_{0.7}\text{Ce}_x\text{CuO}_4$ ( $x = 0.05$ ) sample

Single crystals of PLCCO with  $x = 0.05$  were synthesized by the traveling-solvent floating-zone method. First the sample was protect-annealed at 800 °C for 24 hours and then annealed at 400 °C for 48 hours. Thus annealed crystal showed superconductivity at  $T_c = 24$  K. The magnetic ordering temperature determined from  $\mu\text{SR}$  spectra was 85 K, which is lower than that of the  $x = 0.02$  annealed sample. ARPES spectra of the  $x = 0.05$  sample are displayed in Supplementary Fig. 1. They are qualitatively consistent with those obtained from the  $x = 0.02$  sample.

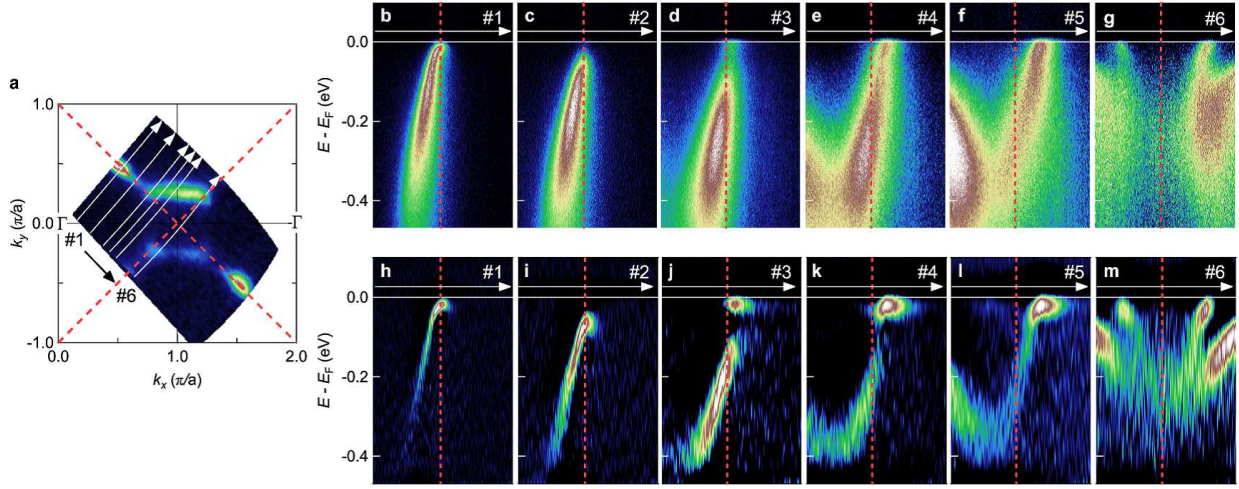
### Supplementary Note 2: Physical properties of protect-annealed $\text{Pr}_{1.3-x}\text{La}_{0.7}\text{Ce}_x\text{CuO}_4$ ( $x = 0.02$ ) samples

Supplementary Fig. 7a shows the resistivity of as-grown and annealed  $\text{Pr}_{1.3-x}\text{La}_{0.7}\text{Ce}_x\text{CuO}_4$  (PLCCO,  $x = 0.02$ ) single crystals. While the as-grown sample is insulating, the protect-annealed sample shows metallic behavior down to  $\sim 50$  K, probably due to the removal of impurity apical oxygen atoms. According to muon-spin-rotation ( $\mu\text{SR}$ ) measurements, the rotation of muons were observed for both samples at low temperatures. The magnetic ordering temperature determined from  $\mu\text{SR}$  spectra, defined as a temperature where magnetic volume fraction develops to 50 %, is 240 K and 140 K for the as-grown and annealed samples, respectively. The  $\mu\text{SR}$  spectra suggest that the AFM order in annealed PLCCO ( $x = 0.02$ ) is not long ranged. The magnetic susceptibility of the annealed sample exhibits hysteresis as shown in Fig. 7b, which is indicative of a spin-glass behavior [1].

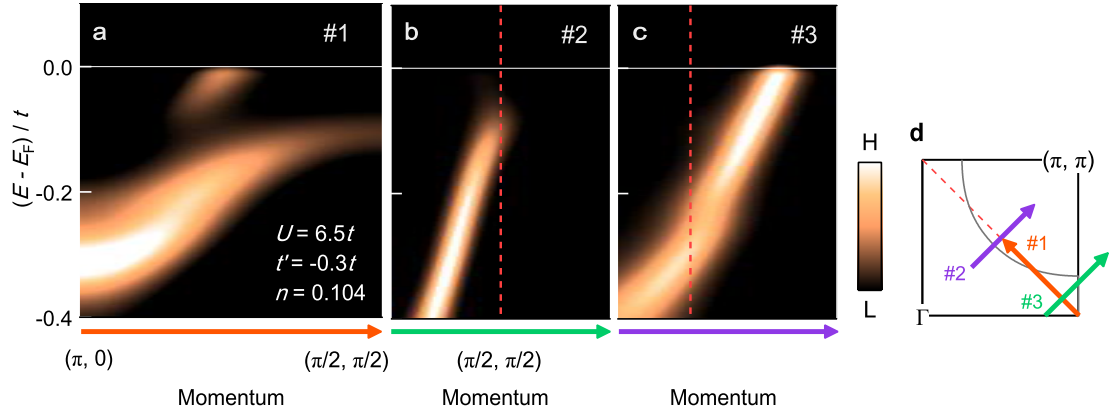
---

[1] Kuroshima, S. *et al.* Phase diagram of the electron-doped superconductor  $\text{Pr}_{1-x}\text{LaCe}_x\text{CuO}_{4-\delta}$ . *Physica C: Superconductivity* **392**, 216 – 220 (2003).

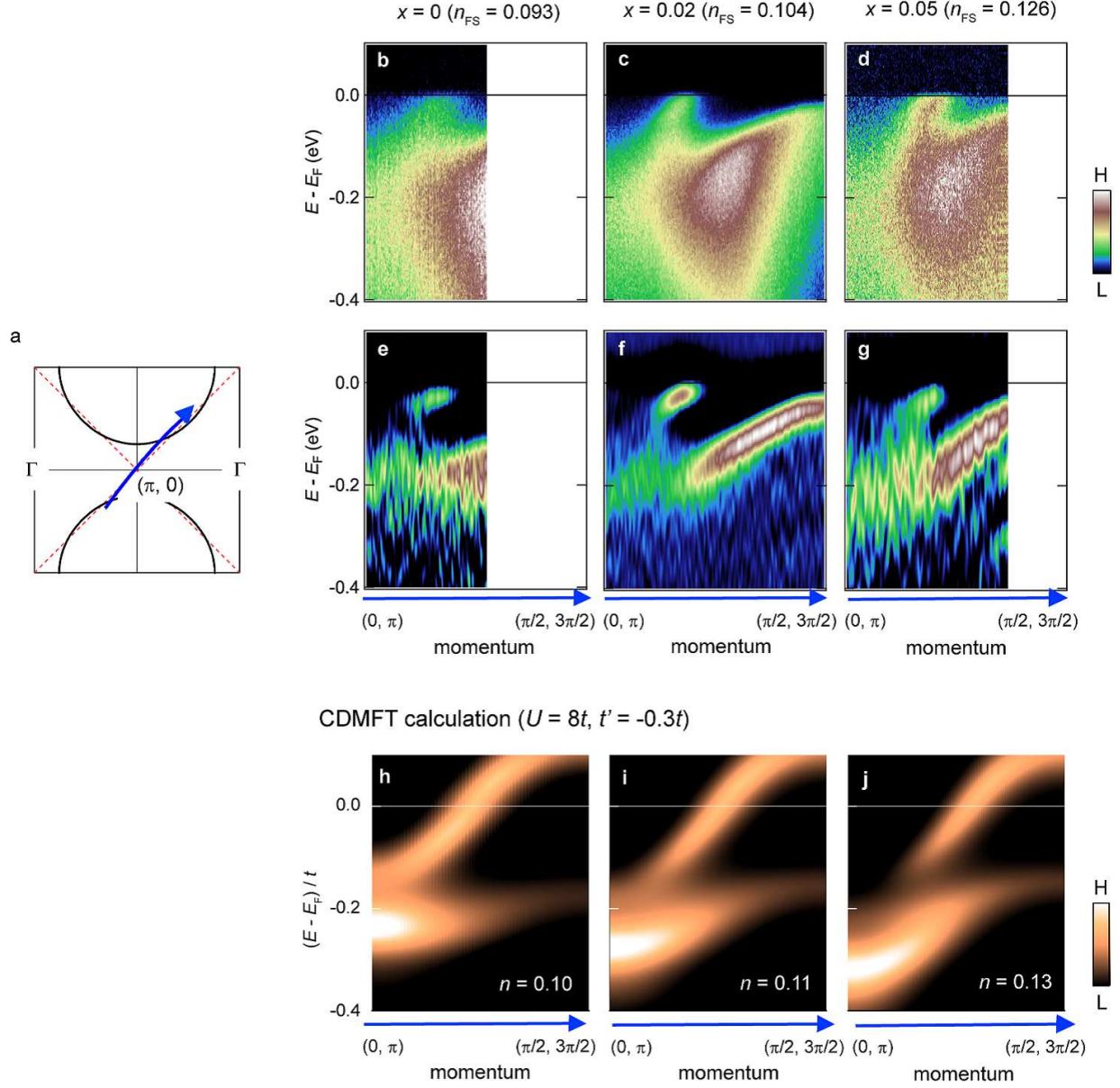
## Supplementary Figures



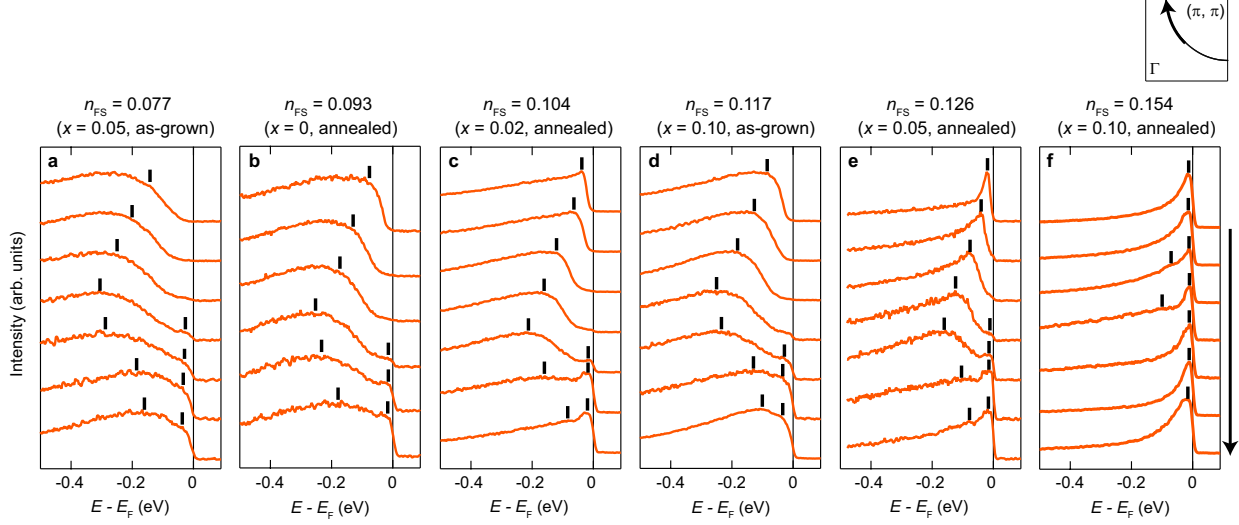
**Supplementary Figure 1: ARPES spectra of a protect-annealed PLCCO ( $x = 0.05$ ) single crystal.** **a**, Fermi surface mapping. Spectral intensity integrated within  $\pm 20$  meV of  $E_F$  is plotted. **b–g**, Band images taken along the cuts indicated in **a**. The AFM BZ boundary is shown by dashed red lines in each panel. **h–m**, Corresponding second derivatives with respect to energy.



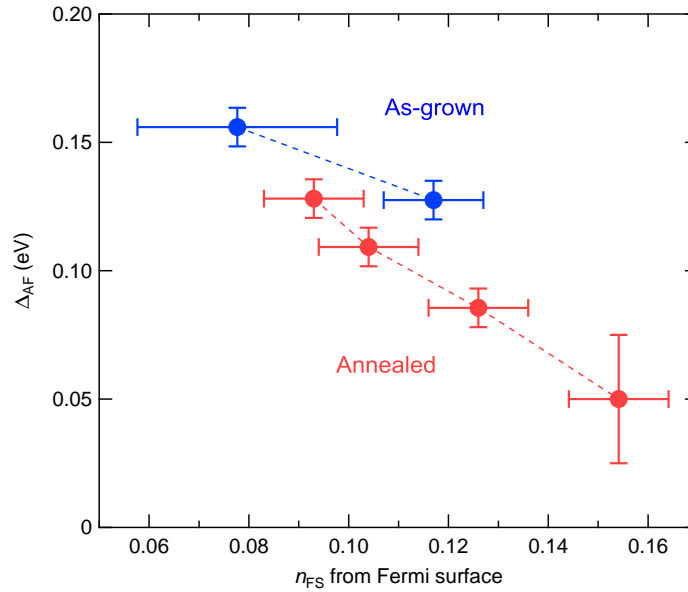
**Supplementary Figure 2: CDMFT calculations conducted with  $U = 6.5t$ .** **a–c**, Calculated spectral function along the cuts #1–#3, respectively, indicated in **d**.



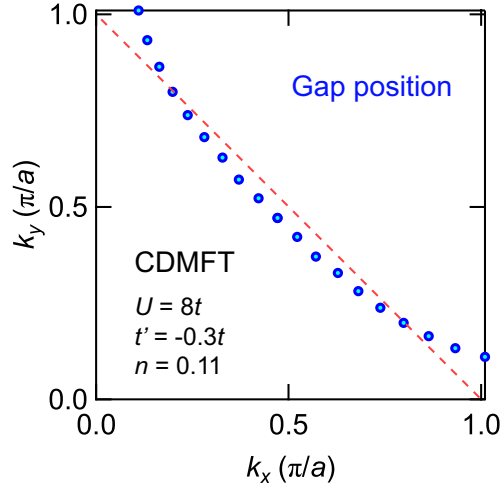
**Supplementary Figure 3: Band dispersion of protect-annealed PLCCO samples along the AF BZ boundary.** **a**, A momentum cut for **b–d** and **e–g**. **b–d**, Band dispersion along the cut indicated in **a** for  $x = 0$ ,  $x = 0.02$ , and  $x = 0.05$  protect-annealed samples, respectively. **e–g**, Second derivative of **b–d** with respect to energy. **h–j**, Spectral function calculated using CDMFT with  $U = 8t$  and  $t' = -0.3t$ . Doped electron concentration  $n$  is 0.10, 0.11, and 0.13, respectively.



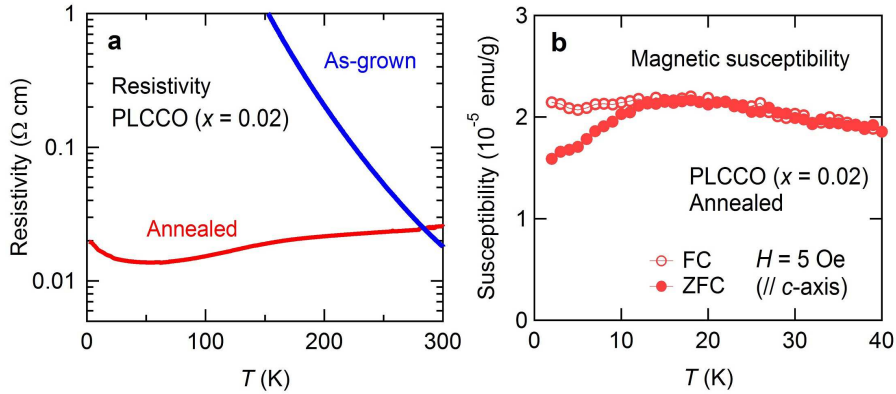
**Supplementary Figure 4: EDCs of PLCCO samples.** a–f, EDCs plotted from nodal to antinodal region for PLCCO samples with different electron concentration  $n_{FS}$  estimated from Fermi surface area. Vertical bars indicates the peak positions.



**Supplementary Figure 5:  $\Delta_{AF}$  versus  $n_{FS}$  for as-grown and protect-annealed PLCCO samples.** See Supplementary Fig. 4 for the correspondence between  $n_{FS}$  and the chemical composition.



Supplementary Figure 6: Gap opening positions for PLCCO ( $x = 0.02$ ) predicted by the CDMFT calculation.



Supplementary Figure 7: Physical properties of PLCCO ( $x = 0.02$ ) single crystals. **a**, Resistivity of as-grown and protect-annealed PLCCO ( $x = 0.02$ ) samples. **b**, Magnetic susceptibility of the annealed PLCCO ( $x = 0.02$ ) sample measured with field cooling (FC) and zero-field cooling (ZFC).